

Electronic properties of zero-line modes in bilayer graphene: An *ab initio* studyZhi Yan ^{1,2}, Tao Hou,² Yulei Han ^{3,2,*}, Xiaohong Xu,^{1,†} and Zhenhua Qiao ^{2,‡}¹*School of Chemistry and Materials Science of Shanxi Normal University & Key Laboratory of Magnetic Molecules and Magnetic Information Materials of Ministry of Education, Research Institute of Materials Science of Shanxi Normal University & Collaborative Innovation Center for Shanxi Advanced Permanent Magnetic Materials and Technology, Linfen 041004, China*²*ICQD, Hefei National Laboratory for Physical Sciences at Microscale, CAS Key Laboratory of Strongly-Coupled Quantum Matter Physics, and Department of Physics, University of Science and Technology of China, Hefei, Anhui 230026, China*³*Department of Physics, Fuzhou University, Fuzhou, Fujian 350108, China* (Received 17 October 2021; revised 10 January 2022; accepted 13 January 2022; published 24 January 2022)

The inversion symmetry breaking in a Bernal-stacked graphene bilayer, e.g., by applying a perpendicular electric field, can open a band gap harboring the quantum valley Hall effect. The different valley Hall topologies induced by a spatially varying electric field lead to the formation of a one-dimensional topological conducting channel, also called the zero-line mode (ZLM), existing at the zero-field region. The ZLMs were theoretically predicted by an atomic model and experimentally realized in bilayer graphene. Although the atomic model has been extensively utilized to investigate the electronic properties of ZLMs, a comprehensive *ab initio* study that precisely characterizes the critical condition of ZLMs is still lacking. In this paper, by employing first-principles method, we systematically investigate the electronic properties in two realistic systems, i.e., bilayer graphene with different types of line defects and with dual-split gates. The characteristics of ZLMs in different systems are demonstrated. Interestingly, we find that bilayer graphene with a pentagon-heptagon type of line defect is the optimal geometry to realize ZLMs due to its minimum critical device width as well as a lower formation energy. Our first-principles study implements the research gap between the atomic model and the experimental realization of ZLMs, and provides a practical scheme for realizing ZLMs in bilayer graphene systems.

DOI: [10.1103/PhysRevB.105.035425](https://doi.org/10.1103/PhysRevB.105.035425)**I. INTRODUCTION**

Graphene is an ideal platform to investigate the nature of massless Dirac fermions [1–3]. The hexagonal structure of graphene harbors two degenerate but inequivalent energy valleys at the corner of the first Brillouin zone. When inversion symmetry is broken, e.g., by a staggered sublattice potential in monolayer graphene, or by a perpendicular electric field in a Bernal-stacked graphene bilayer [4–7], the valley contrasting Berry curvature and orbital magnetic moment can be applied to valleytronics [8]. When the mass term of the Dirac fermion changes sign in real space, a one-dimensional topologically confined state, also known as the zero-line mode (ZLM), exists at the zero-field region [9–11]. Due to their topological nature, the ZLMs are robust against backscattering, exhibiting zero bending resistance and long mean free paths on the order of hundreds of micrometers [12,13]. Experimentally, the ZLMs have been observed in bilayer graphene (BLG) with line defects [14,15] and with precise gate alignment [13,16,17], classic graphenelike wave systems [18–21], and twisted bilayer graphene with trigonal network geometry [22–28].

Theoretically, the ZLMs in graphene systems are extensively studied by employing a low-energy method or tight-binding model [9,10,29–49]. Although the results obtained from these methods are qualitatively consistent with experimental observations, it is difficult to use these models to quantitatively describe the electronic properties of ZLMs especially in defective graphene because of the complicated estimation of the model parameters. Moreover, the optimal geometry of line defects in graphene for realizing ZLMs is still not clear. Compared with theoretical models, the first-principles method, as a crucial link between theoretical models and experiments, is more accurate in characterizing all types of ZLMs, hence a systematically first-principles study of ZLMs is highly desired.

In this paper, we theoretically investigate the electronic properties of ZLMs in bilayer graphene by performing first-principles calculations. We investigate two typical systems, i.e., bilayer graphene with line defects and with dual-split gates. In the former case, three types of representative line-defect configurations, i.e., pentagon-octagon (5-8), pentagon-heptagon (5-7), and pentagon-quadrilateral-decagon (5-4-10), are considered. In the presence of a uniform external electric field, we demonstrate that ZLMs can be observed in the three defective bilayer graphene systems with different wave-function distributions. In the latter case, the electronic band structures and wave-function distributions of ZLMs as functions of junction width and gate voltage are comprehensively illustrated. Moreover, compared with

*Corresponding author: hanyulei@ustc.edu.cn

†Corresponding author: xuxh@sxnu.edu.cn

‡Corresponding author: qiao@ustc.edu.cn

bilayer graphene with dual-split gates, we find that bilayer graphene with a line defect more easily forms ZLMs because of the shorter required device width, and the 5-7 line-defect geometry presents the minimum critical device width. Our results reveal that graphene with a line defect is a superior system for realizing ZLMs because of its narrower wave-function broadening of ZLMs and independence of precise alignment of the gates as implemented in Bernal-stacked bilayer graphene. Our comprehensive studies build a bridge between the atomic model and the experimental realization of ZLMs in bilayer graphene systems, and may further promote the feasible realization of ZLMs in experiments.

The rest of this paper is organized as follows. In Sec. II we describe the details of the calculation. Section III describes our results for ZLMs in bilayer graphene with different types of line defects and with dual-split gates, and the optimal geometry for the realization of ZLMs. Section IV summarizes our work. Some auxiliary materials are given in the Appendixes.

II. COMPUTATIONAL METHODS

Our first-principles calculations were performed by using density functional theory (DFT) as implemented in the NANODCAL package [50,51], which can treat a system with thousands of atoms. The double zeta polarized basis set was used to treat the wave function, and the generalized gradient approximation of the Perdew-Burke-Ernzerhof type was used to treat the exchange-correlation interaction [52,53]. The plane-wave cutoff energy was set to 80 hartree. The Brillouin zone was sampled with a k mesh of $1 \times 15 \times 1$, $9 \times 1 \times 1$, and $1 \times 9 \times 1$ for zigzag-, armchair-terminated, and line-defect BLG nanoribbons, respectively. In the self-consistent calculation, the energy convergence criterion was set to 10^{-4} eV. A vacuum space of 20 Å was used in the non-periodic direction of the graphene nanoribbons. The precise line-defect geometries were optimized by using the Vienna *ab initio* simulation package [54–56]. The dangling bonds of carbon atoms were saturated with hydrogen atoms. An experimental BLG interlayer distance of 3.4 Å was adopted in our calculations.

III. RESULTS AND DISCUSSION

A. The ZLMs in bilayer graphene with line defect

The line-defect geometry in bilayer graphene provides a feasible platform to realize ZLMs as experimentally observed [14,15]. However, the specific structure of the line defect is still unclear and requires further experimental characterization. To explore the role of line defects in the formation of ZLMs, we take three types of representative line-defect configurations [57–59], i.e., 5-8, 5-7, and 5-4-10 line defects, as displayed in Figs. 1(b)–1(d). The line defect is only considered in the top layer as experimentally implemented [14], leading to an AB- (BA-) stacked bilayer in the left (right) side of the line defect. Therefore, when a uniform external electric field is applied as shown in Fig. 1(a), the regions separated by the line defect harbor different valley Hall topologies to form ZLMs.

Figures 1(e)–1(g) display the band structures of the three types of line defects in the absence of an external electric field. One can find that these systems display metallic behavior at E_F due to the presence of gapless edge states as denoted in blue. The line defect also contributes an electronic state connecting valley K and K' as displayed in green. It is noteworthy that both the gapless edge states and line-defect states are topologically trivial, indicating that these states can be easily destroyed by short-range disorders.

When an external electric field is applied, as displayed in Figs. 1(h)–1(j), one can observe that a bulk band gap opens due to the absence of inversion symmetry, and two pairs of ZLMs exist separately inside the bulk band gap at valley K/K' as displayed in red. We can find that the propagating directions of ZLMs at valley K and valley K' are opposite because of the different sign of the electronic group velocities of ZLMs at valleys K/K' . The ZLMs are topologically nontrivial states due to the nonzero Berry curvature distributions around valley K/K' [8], and the backscattering of ZLMs is prohibited because of the large valley separation between forward- and backward-propagating electronic states. Although the gapless edge and line-defect states are still present inside the bulk gap, they can be readily destroyed by external disorders. Therefore, only ZLMs are robust against disorders and can survive due to their topological nature.

We further investigate the wave-function distributions of ZLMs at valley K , whereas the case at valley K' can be readily obtained because of the presence of time-reversal symmetry. Figure 2 displays the real-space wave-function distributions of ZLMs [labeled as A and B states in Figs. 1(h)–1(j)]. One can observe that the wave functions of the two ZLMs are mainly localized around the line-defect regions for different types of defect geometries, and the distributions in the line-defect (top)/pristine (bottom) layers of each mode are asymmetric due to the different geometries of the two layers. Although the wave functions of mode A and mode B are not exactly same, they display a general trend, i.e., the broadening of line-defect layer is smaller than that of pristine layer, implying that the line defect is beneficial to the formation and detection of ZLMs. In addition to the states from ZLMs, we also study the wave-function distributions of edge states and line-defect states in Fig. 7 in Appendix A. One can find an explicit distinction between ZLMs and edge/line-defect states, i.e., edge/line-defect states are strongly localized with sharp peaks in wave function, whereas ZLMs are more broadened. This distinction indicates that localized states of an edge/line defect are easier to be destroyed by weak disorder whereas the broadened states of ZLMs are more robust against disorders, which is consistent with the aforementioned discussion.

B. The ZLMs in dual-gated perfect BLG

Besides line-defect geometry, a more direct but challenging way to realize ZLMs in bilayer graphene is by utilizing precise dual-split-gated alignment as experimentally implemented [13,16,17]. Figure 3(a) displays the schematic plot of the dual-split-gated device, where opposite electric fields are applied on the left/right sides of bilayer graphene with a tunable junction width of w . In the absence of an electric field, as displayed in Fig. 3(b), two pairs of degenerate boundary

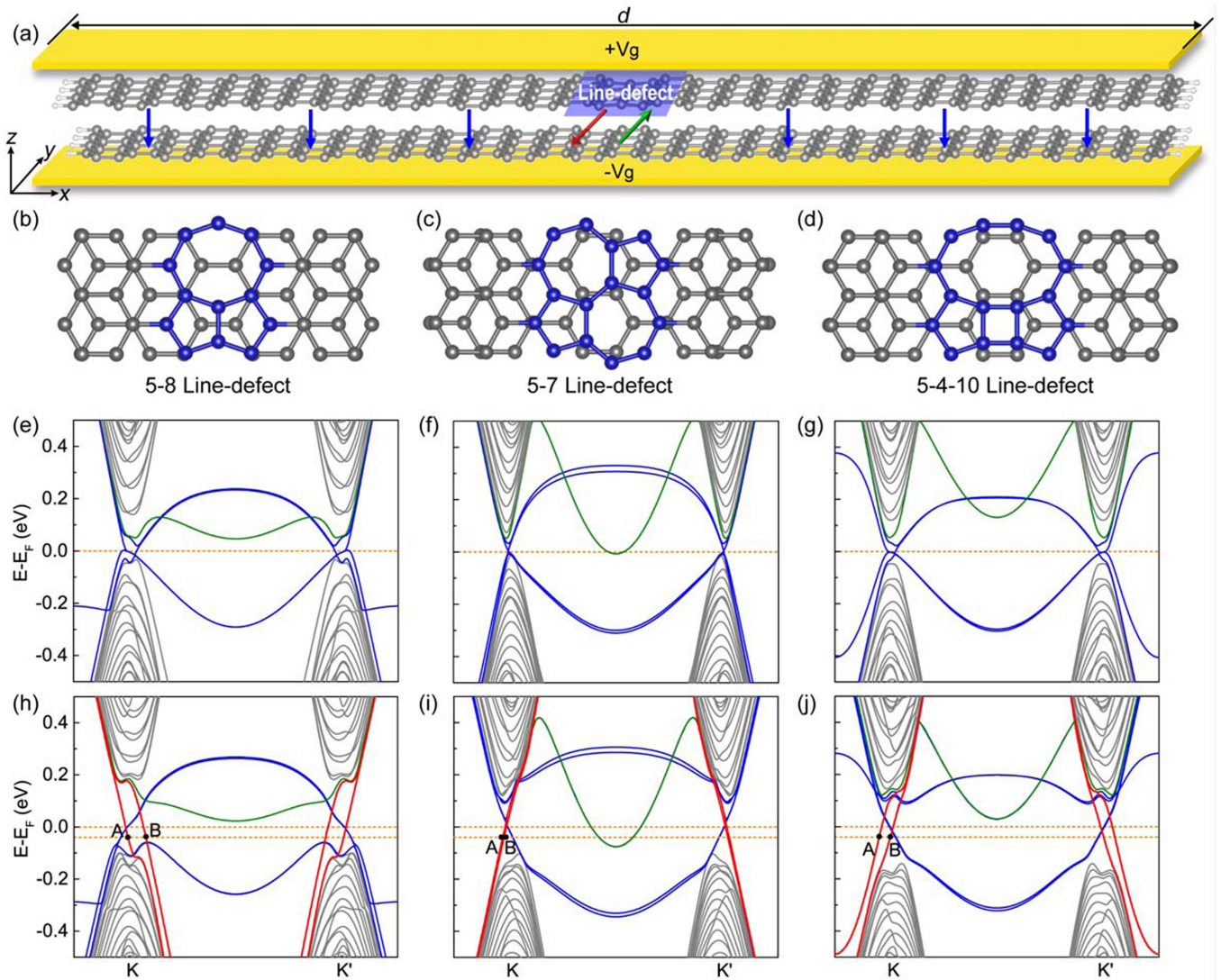


FIG. 1. (a) Schematic plot of a gated line-defect BLG device with width d . The perpendicular electric field is denoted by vertical blue arrows. The green and red arrows represent ZLMs from valley K and K' , respectively. The potential difference between the top and bottom gates is $U = 2V_g$. The blue shaded area on the top layer represents the line-defect structure. (b)–(d) Three different types of line-defect BLG structures: (b) pentagon-octagon (5-8) line defect; (c) pentagon-heptagon (5-7) line defect; (d) pentagon-quadrilateral-decagon (5-4-10) line defect. (e)–(i) The corresponding band structures of zigzag-terminated line-defect BLG ribbons (e)–(g) without and (h)–(j) with applying an external electric field ($U = 10$ V). The red, green, and blue bands denote ZLMs, edge states, and line-defect states, respectively. The Fermi level is set to zero. The zero-line modes originate from the different valley Hall topologies induced by a spatially varying electric field. The line-defected bilayer graphene leads to an AB- (BA-) stacked bilayer in the left (right) side of the line defect harboring different valley Hall topologies. Therefore, applying a uniform external electric field can naturally induce zero-line modes.

states connecting valley K and valley K' exist at zigzag edges. In the presence of a uniform electric field ($U_{\text{left}} = U_{\text{right}}$), as shown in Fig. 3(c), a bulk band gap appears and each degenerate boundary state inside the bulk gap split into two nondegenerate states because of the broken inversion symmetry of bilayer graphene. When electric fields in the left/right regions are opposite ($U_{\text{left}} = -U_{\text{right}}$), as shown in Fig. 3(d), two pairs of counterpropagating ZLMs (marked in red) exist in valleys K and K' due to the different Hall topologies of the left/right regions.

We then turn to study the wave-function distribution of ZLMs labeled as A–D in Fig. 3(d). Figure 4 displays the corresponding wave-function distributions with a Fermi energy of $E = -0.08$ eV. We can find that, different from

the line-defect case, each mode is symmetrically distributed in the top and bottom layers. However, the distributions of two modes in each valley are not identical mainly due to a small momentum separation, whereas the distributions of two modes with the same momentum separation to valley K/K' are identical. For example, modes A and B at valley K display different distributions, but modes A (B) at valley K and D (C) at valley K' show the same distributions because of their same momentum separation to valley K and K' . We also plot the distribution of edge states inside the bulk band gap to compare it with ZLMs (see Fig. 8 in Appendix A), which shows extremely sharp peaks at the boundary of the nanoribbon. Moreover, in an armchair-terminated graphene nanoribbon, ZLMs display similar

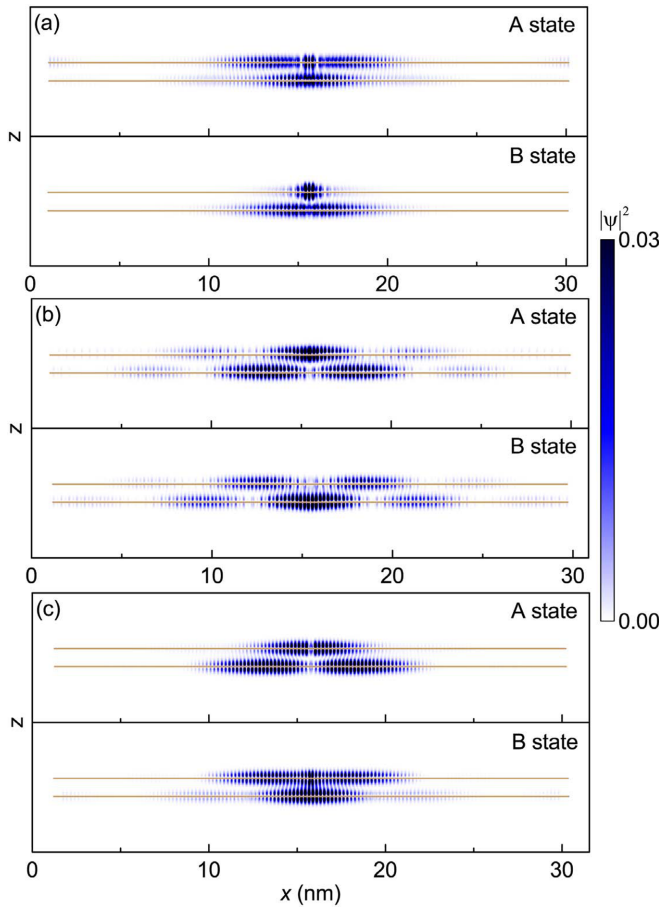


FIG. 2. The real-space wave-function distributions of ZLMs [labeled as A and B states in Figs. 1(h)–1(j)] at $E = -0.04$ eV for the (a) 5-8 line defect, (b) 5-7 line defect, and (c) 5-4-10 line defect. The horizontal lines represent the graphene plane.

wave-function distributions (see Fig. 9 in Appendix B). Our previous work studied the ZLMs in dual-split-gated bilayer graphene based on the tight-binding model [38]. In general, the results of DFT are consistent with the tight-binding model. In more detail, the complete inconsistency in the shape of the zigzag boundary state is mainly due to the fact that the atomic model ignores the structural relaxation. In addition, for the setting of the interlayer potential difference, the tight-binding model uses the AB sublattice potential to simulate the actual gate application, and $2U$ is the guessed value directly acting on the C atoms. Therefore, the results of DFT are more instructive to the experiments.

The above calculations consider a zero junction width ($w = 0$). Experimentally, it is challenging to fabricate a device with a seamless connection of the left/right electric gates, hence it is essential to investigate the evolution of ZLMs with w . Figure 5 displays band structures near valley K and the corresponding wave-function distributions of ZLMs with different junction widths w . When w is small, as demonstrated in Figs. 5(a)–5(c), band structures of ZLMs marked in red continuously change around valley K inside the bulk gap, indicating the absence of coupling between ZLMs and edge states. When w is large, as shown in Figs. 5(d)–(f), one can observe that band structures of

ZLMs near the Fermi level are discontinuous and are hybrid with edge states, implying that coupling between ZLMs and edge states may destroy the completeness and topology of ZLMs. The above analysis can be further approved by wave-function distributions of ZLMs. Figures 5(g)–5(j) display wave-function distributions of mode A labeled in Figs. 5(a)–5(f) with the increase of junction width w . We can find that the distributions in the top and bottom layers are always symmetric regardless of the variation of w . When $w = 0$ [see Fig. 5(g)], ZLM is well distributed in the middle of a graphene nanoribbon with Gaussian form. The increase of w not only broadens the wave functions in a wider range, but also forms more complicated distributions with an M shape. As displayed in Figs. 5(i) and 5(j), the larger w makes the broadening of wave function extend to the nanoribbon edge, indicating the appearance of coupling between ZLMs and edge states that is consistent with band structures. Moreover, we can find that the bulk band gap reduces with the increase of w because of the larger zero-gating regions. Therefore, small junction width is beneficial to experimentally observe ZLMs.

C. The optimal geometry for realization of ZLMs

In above two sections, we have studied the electronic properties of ZLMs in two systems, i.e., BLG with line-defect geometry and with precise dual-split-gate alignment. A crucial question arises: Which system is easier to realize ZLMs? Here, we quantitatively investigate this issue by performing elaborate first-principles calculations. We utilize wave-function distributions of ZLMs to determine the critical device width d_c of devices. The procedure can be summarized as follows: (i) Fix a sufficiently large device width d , i.e., $d = 34.02, 33.45, 36.51,$ and 32.83 nm for dual-split-gate BLG, 5-8 line defect, 5-7 line defect, and 5-4-10 line defect, respectively; (ii) calculate the wave functions of ZLMs at certain U ; (iii) determine the critical device width from the fixed wave-function broadening; (iv) change the gate voltage from 7 to 16 V and then repeat steps (ii) and (iii).

Figure 6 displays the critical device width d_c for different BLG systems as a function of interlayer potential difference U . When U increases, the spread of the wave-function distribution gradually decreases, leading to reduced d_c , e.g., the critical device width for dual-split-gated BLG decreases from 30.82 to 20.05 nm when the interlayer potential difference increases from 7.0 to 16.0 V. Most importantly, the critical device width for BLG with a line defect is smaller by about 20%–30% than that with dual-split gate, indicating that line-defect geometry is more beneficial to experimentally realize ZLMs at a given electric field. In the three types of line-defect geometries, BLG with 5-7 line defect displays the lowest d_c . In addition, previous studies have shown that the 5-7 type of topological defect has the lowest formation energy, indicating that this type of defect can be feasibly induced in experiments [60]. Therefore, BLG with a line defect is much easier to realize ZLMs than BLG with a dual-split gate, and a system with a 5-7 type of line defect is the optimal geometry for the realization of ZLMs.

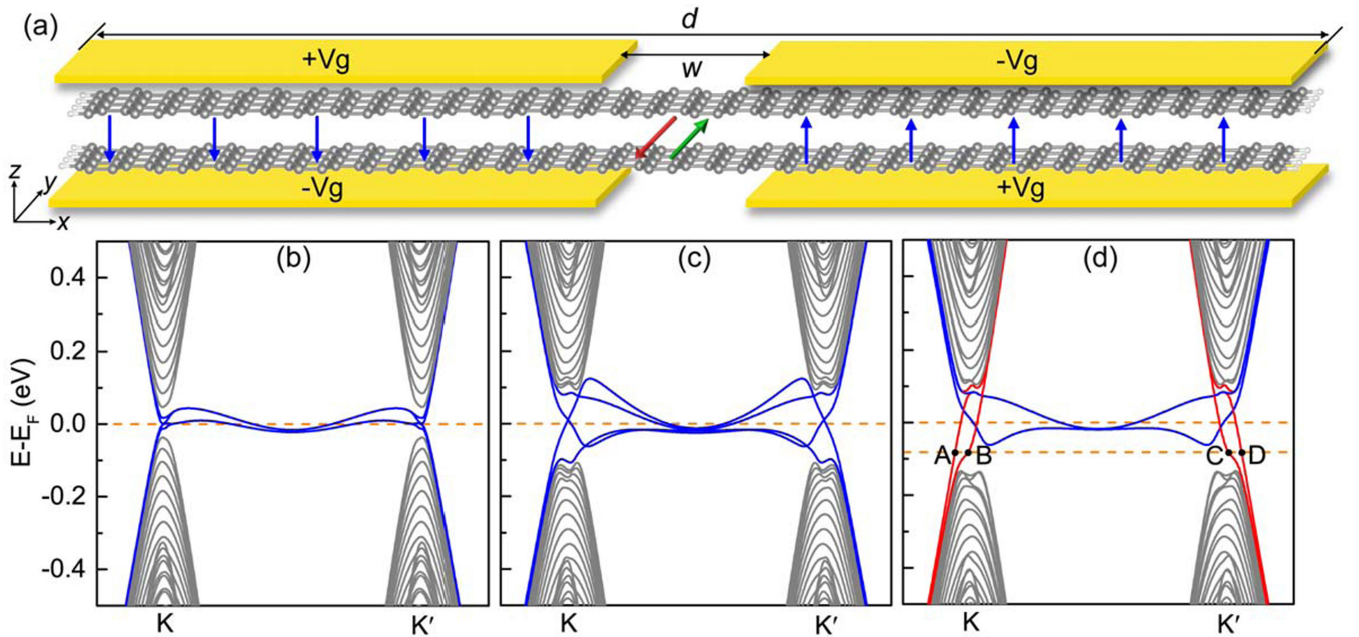


FIG. 3. (a) Schematic plot of a dual-split-gated bilayer graphene (BLG) device with width d . The perpendicular electric field is denoted by vertical blue arrows. The green and red arrows represent ZLMs from valley K and K' separately. The junction width is denoted by w . (b)–(d) Band structures of zigzag-terminated BLG ribbons (b) in the absence of an electric field, (c) in the presence of a uniform electric field, and (d) opposite electric field. The system parameters are $d = 34.02$ nm, $U = 10$ V, and $w = 0$. The red and blue bands respectively represent ZLMs and edge states. The Fermi level is set to zero.

IV. SUMMARY

In conclusion, we have systematically studied the electronic properties of ZLMs in different BLG systems by implementing *ab initio* calculations. In BLG with different types of line defects, i.e., 5-8, 5-7, and 5-4-10 line defects, ZLMs can be realized by applying a uniform electric field. The wave functions demonstrate different distribution forms

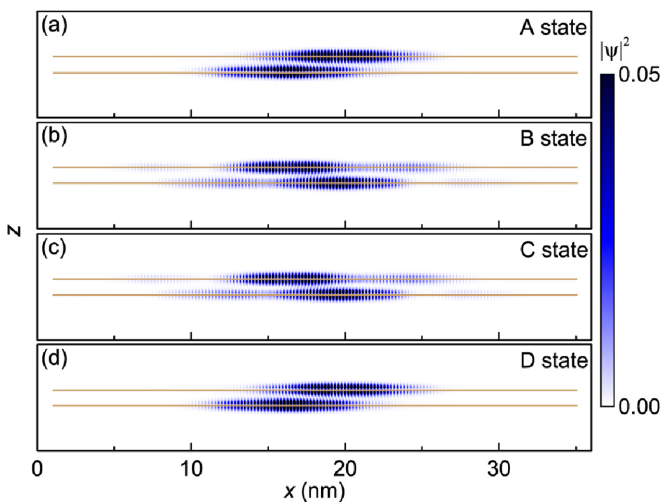


FIG. 4. The real-space wave-function distributions of ZLMs [labeled as A, B, C, and D in Fig. 3(d)] at $E = -0.08$ eV. (a)–(d) denote modes A–D of zigzag boundary BLG with $E_F = -0.08$ eV. The horizontal lines represent the graphene plane.

at the top and bottom layers. In BLG with dual-split gates, we find that the junction width is crucial in determining the wave-function distributions of ZLMs. Most importantly, we quantitatively find that the critical device width for the line-defect geometry in realizing ZLMs is much smaller than that for dual-split-gated BLG, indicating that the line-defect geometry is more beneficial to realize ZLMs. Among these line defects, we find that the 5-7 type has the smallest critical device width, indicating that the 5-7 line defect is the optimal geometry for realizing ZLMs in a BLG system. Our work not only bridges a crucial link between atomic models and experiments about ZLMs, but also provides detailed pictures to stimulate more experimental realizations of ZLMs.

The different types of line defects are feasible to be experimentally realized. For example, 5-8 line-defected graphene can be obtained by using the chemical vapor deposition (CVD) method on a Ni(111) substrate [58]. The molecular dynamics simulation also proved that such a 5-8 line defect can be spontaneously formed from defects in the graphene sheet at a high temperature [61]. The 5-7 line-defected graphene can be obtained by using CVD grown on copper foils [62]. For the 5-4-10 line defect, it can be fabricated in suspended monolayer graphene using controlled focused electron beam irradiation [63] and the on-surface method [64].

ACKNOWLEDGMENTS

This work was financially supported by the National Natural Science Foundation of China (No. 11974327, No. 12004369, and No. 51871137), Fundamental Research

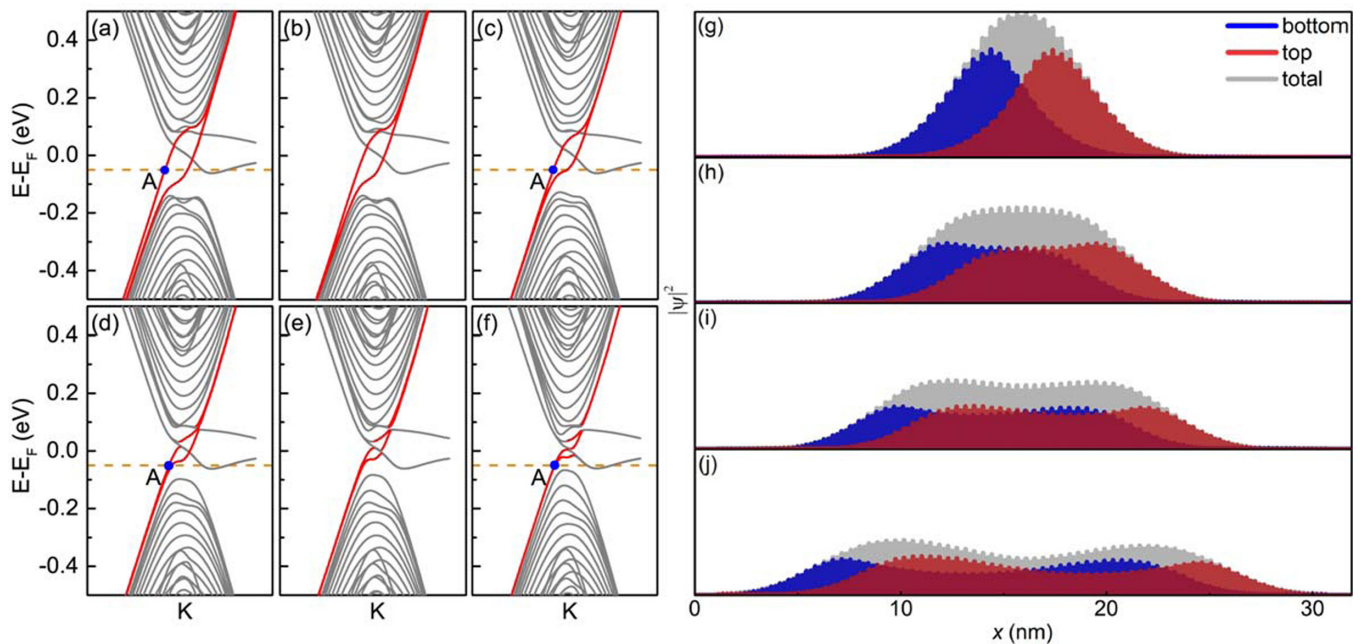


FIG. 5. (a)–(f) Band structures of zigzag-terminated BLG with different junction widths w . (a) $w = 0$ nm; (b) $w = 2.89$ nm; (c) $w = 6.37$ nm; (d) $w = 10.61$ nm; (e) $w = 12.73$ nm; (f) $w = 15.91$ nm. The ribbon width d is 29.76 nm, and the interlayer potential difference U is 10 V. (g)–(j) The wave-function distributions of the mode A [labeled in (a), (c), (d), and (f)] with different junction widths w at $E = -0.05$ eV. The red, blue, and gray areas represent the wave functions of the top, bottom layer, and sum over of two layers, respectively.

Funds for the Central Universities (WK3510000010, WK2030020032), China Postdoctoral Science Foundation (2020M681998), and Anhui Initiative in Quantum Information Technologies (Grant No. AHY170000). We are grateful to AM-HPC and Supercomputing Center of USTC for providing the high-performance computing resources. Z.Y. was partially supported by the Graduate Science and Technology Innovation Project Foundation of Shanxi Normal University (No. 2021XBY004).

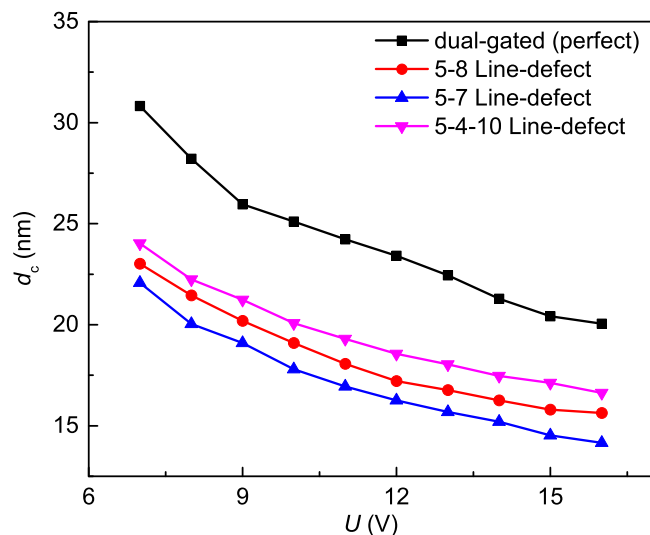


FIG. 6. The critical device width d_c for realizing ZLMs with different geometries as a function of interlayer potential difference U .

APPENDIX A: WAVE-FUNCTION DISTRIBUTIONS OF EDGE/LINE-DEFECT STATES

To further identify the states (E, F, G, H, and I) other than ZLMs inside the bulk band gap, we calculated the wave-function distribution of these states at the high-symmetry point G , as shown in Figs. 7(g)–7(i). Obviously, for all line-defect systems, the E, F, G, and H states are distributed at the boundary of BLG, while the I state falls in the middle of BLG and is located at the line defect of the top graphene layer (see inset figures), indicating that the E, F, G, and H states are boundary edge states [marked in blue in Figs. 7(a)–7(f)] and the I state (marked in green) is the trivial impurity state contributed by atoms at the line defect.

We also calculated the wave-function distribution of the edge states of perfect AB-stacked zigzag-terminated BLG at the high-symmetry point X . As shown in Fig. 8(c), all E, F, G, and H states are distributed at the boundary of both sides of the sample, suggesting that these states marked in blue in Figs. 8(a) and 8(b) are edge states.

APPENDIX B: ZLMs IN ARMCHAIR-TYPE GRAPHENE RIBBON

The ZLMs can also be obtained in armchair-terminated BLG with opposite electric field polarities. As shown in Figs. 9(a) and 9(b), the armchair-terminated BLG is conductive in the absence of an electric field, and a large band gap appears in the presence of an electric field due to the effect of interlayer potential difference. When an opposite electric field is applied to both sides of the BLG, nontrivial ZLMs (marked in red) appear in the bulk band gap in Fig. 9(c). The

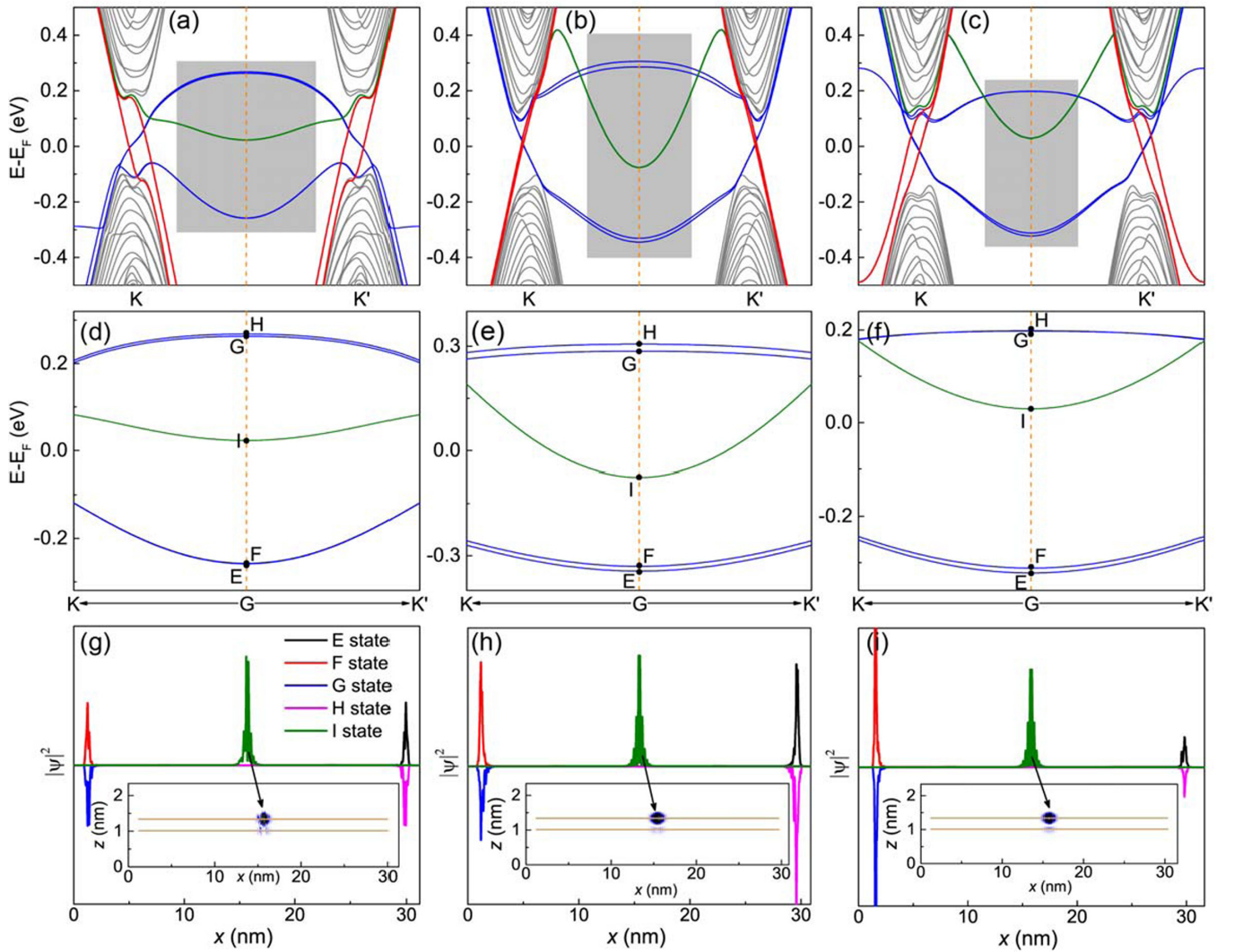


FIG. 7. (a)–(c) Band structures of a line-defect BLG ribbon in the presence of an uniform electric field ($U = 10$ V). (d)–(f) The local band structures [see the gray shaded rectangle in (a)–(c)] of line-defect BLG ribbon with $U = 10$ V. (g)–(i) Wave-function distributions of the states E, F, G, H and I [as labeled in (d)–(f)] at the high-symmetry point G for the line-defect BLG ribbons. The inset represents the real-space wave-function distribution. The first, second, and third columns are respectively for 5-8, 5-7, and 5-4-10 line defects.

difference between different boundaries is that the edge states appear at the zigzag boundary BLG ribbon, while there are no edge states in the armchair boundary ribbon. The wave

functions of these ZLMs (A, B, C, and D) are distributed in the middle of the BLG, which verifies that they are ZLMs as shown in Fig. 9(d).

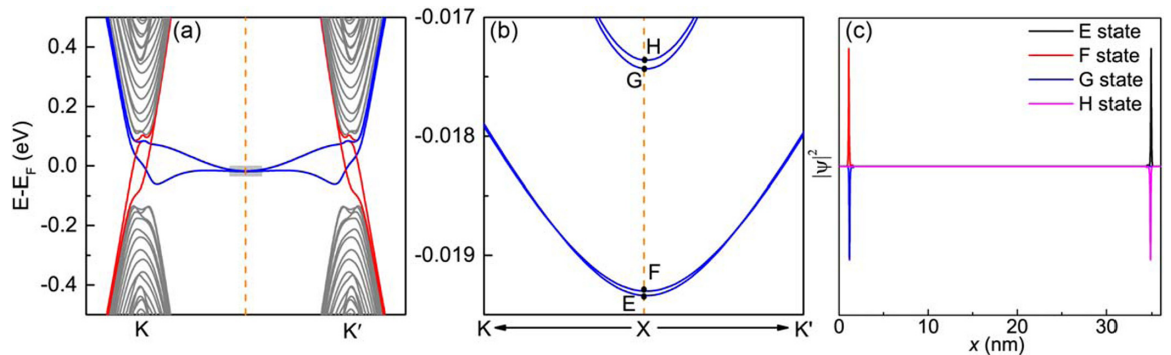


FIG. 8. (a) Band structures of zigzag-terminated BLG ribbons with $U = 10$ V and $w = 0$ ($d = 34.02$ nm). (b) The local band structures [see the gray shaded rectangle in (a)] of an AB-stacked BLG ribbon with a zigzag boundary. (c) The wave-function distributions of the edge states E, F, G, and H [as labeled in (b)] at the high-symmetry point X .

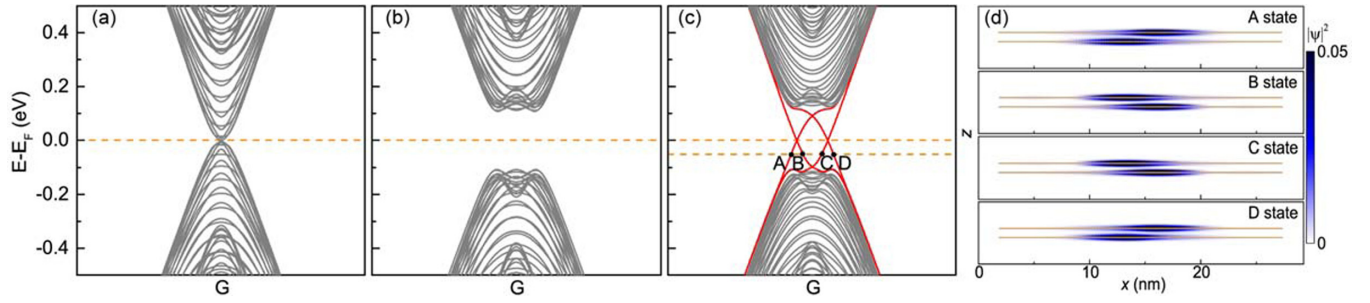


FIG. 9. (a)–(c) Band structures of armchair-terminated BLG ribbons with $U = 10$ V and $w = 0$ ($d = 27.25$ nm). (a) Without an electric field; (b) with a uniform electric field; (c) with opposite electric field. The red and blue bands are the ZLMs and edge states, respectively. The Fermi level is set to zero. (d) The wave-function distributions of four (A, B, C, D) ZLMs [as (c)] at the selected Fermi level ($E = -0.05$ eV) in real space. The two brown horizontal lines represent BLG.

APPENDIX C: COMPARED WITH TIGHT-BINDING MODEL

Based on atomic models, the ZLMs in a realistic bilayer graphene with line-defect geometry have yet to be reported. But there are some related works using tight-binding model to study the electronic properties of ZLMs in dual-split-gated bilayer graphene systems [9,12,13,38]. To directly compare our results with that from the tight-binding model calculations, we calculated the electronic properties and the wave functions of ZLMs in dual-split-gated bilayer graphene with a zigzag boundary by employing the tight-binding model. The tight-binding Hamiltonian can be written as

$$H = -t \sum_{(i,j)} (c_i^\dagger c_j + \text{H.c.}) - t_\perp \sum_{(i \in T, j \in B)} (c_i^\dagger c_j + \text{H.c.}) + \sum_{i \in T} U_i c_i^\dagger c_i - \sum_{i \in B} U_i c_i^\dagger c_i, \quad (\text{C1})$$

where c_i^\dagger (c_i) is the electron creation (annihilation) operator on site i . The first and second terms represent the intralayer and interlayer nearest-neighbor hopping, respectively, with

hopping amplitudes of $t = 2.6$ eV and $t_\perp = 0.34$ eV. The third and fourth terms indicate the site energies at the top and bottom layers, respectively. In the part on the left (right), the on-site energy U_i is constant at $+U$ (U). The selections of the device width d and the junction width w are consistent with the DFT parameters. To obtain a bulk band gap comparable to the first-principles calculations, we tested the value of U and finally set it to be $U = 0.1$ eV. The results from the tight-binding model are shown in Fig. 10.

In general, the results from first-principles calculations are consistent with that from the tight-binding model. Two minor differences are (i) the shape of the zigzag boundary state [see Figs. 3(d) and 10(a)], which is mainly due to the fact that the atomic model ignores the structural relaxation; (ii) the wave function of ZLMs obtained by the tight-binding model has a larger broadening than that from first-principles calculations [see Figs. 5(a) and 10(b)], which is mainly due to the not exactly equal interlayer potential difference (the AB sublattice potential in the tight-binding model, and gate voltage in first-principles calculations). Therefore, the results from first-principles calculations are more instructive to the experiments.

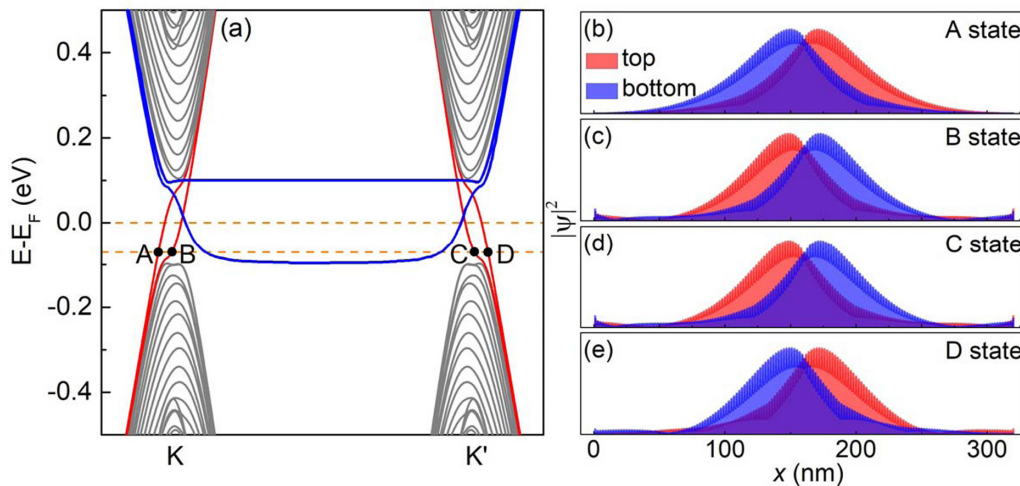


FIG. 10. Calculational results of tight-binding model. (a) Band structures of a BLG ribbon with opposite electric fields in the adjoining regions. (b)–(d) Corresponding wave-function distributions of ZLMs [A–D states, labeled in (a)].

- [1] K. S. Novoselov, A. K. Geim, S. V. Morozov, D. Jiang, Y. Zhang, S. V. Dubonos, I. V. Grigorieva, and A. A. Firsov, *Science* **306**, 666 (2004).
- [2] K. S. Novoselov, A. K. Geim, S. V. Morozov, D. Jiang, M. I. Katsnelson, I. V. Grigorieva, S. V. Dubonos, and A. A. Firsov, *Nature (London)* **438**, 197 (2005).
- [3] Y. B. Zhang, Y. W. Tan, H. L. Stormer, and P. Kim, *Nature (London)* **438**, 201 (2005).
- [4] E. McCann, *Phys. Rev. B* **74**, 161403(R) (2006).
- [5] H. K. Min, B. Sahu, S. K. Banerjee, and A. H. MacDonald, *Phys. Rev. B* **75**, 155115 (2007).
- [6] E. V. Castro, K. S. Novoselov, S. V. Morozov, N. M. R. Peres, J. M. B. Lopes dos Santos, J. Nilsson, F. Guinea, A. K. Geim, and A. H. Castro Neto, *Phys. Rev. Lett.* **99**, 216802 (2007).
- [7] Y. Zhang, T. T. Tang, C. Girit, Z. Hao, M. C. Martin, A. Zettl, M. F. Crommie, Y. R. Shen, and F. Wang, *Nature (London)* **459**, 820 (2009).
- [8] D. Xiao, W. Yao, and Q. Niu, *Phys. Rev. Lett.* **99**, 236809 (2007).
- [9] I. Martin, Y. M. Blanter, and A. F. Morpurgo, *Phys. Rev. Lett.* **100**, 036804 (2008).
- [10] G. W. Semenoff, V. Semenoff, and F. Zhou, *Phys. Rev. Lett.* **101**, 087204 (2008).
- [11] R. Jackiw and C. Rebbi, *Phys. Rev. D* **13**, 3398 (1976).
- [12] Z. H. Qiao, J. Jung, Q. Niu, and A. H. MacDonald, *Nano Lett.* **11**, 3453 (2011).
- [13] J. Li, K. Wang, K. J. McFaul, Z. Zern, Y. F. Ren, K. Watanabe, T. Taniguchi, Z. H. Qiao, and J. Zhu, *Nat. Nanotechnol.* **11**, 1060 (2016).
- [14] L. Ju, Z. W. Shi, N. Nair, Y. C. Lv, C. H. Jin, J. Velasco, Jr., C. Ojeda-Aristizabal, H. A. Bechtel, M. C. Martin, A. Zettl, J. Analytis, and F. Wang, *Nature (London)* **520**, 650 (2015).
- [15] L. J. Yin, H. Jiang, J. B. Qiao, and L. He, *Nat. Commun.* **7**, 11760 (2016).
- [16] J. Li, R. X. Zhang, Z. X. Yin, J. X. Zhang, K. Watanabe, T. Taniguchi, C. Liu, and J. Zhu, *Science* **362**, 1149 (2018).
- [17] H. Chen, P. J. Zhou, J. W. Liu, J. B. Qiao, B. Oezylmaz, and J. Martin, *Nat. Commun.* **11**, 1202 (2020).
- [18] S. S. Sunku, G. X. Ni, B. Y. Jiang, H. Yoo, A. Sternbach, A. S. McLeod, T. Stauber, L. Xiong, T. Taniguchi, K. Watanabe, P. Kim, M. M. Fogler, and D. N. Basov, *Science* **362**, 1153 (2018).
- [19] J. W. Dong, X. D. Chen, H. Zhu, Y. Wang, and X. Zhang, *Nat. Mater.* **16**, 298 (2017).
- [20] F. Gao, H. R. Xue, Z. J. Yang, K. Lai, Y. Yu, X. Lin, Y. D. Chong, G. Shvets, and B. L. Zhang, *Nat. Phys.* **14**, 140 (2018).
- [21] J. Y. Lu, C. Y. Qiu, L. P. Ye, X. Y. Fan, M. Z. Ke, F. Zhang, and Z. Y. Liu, *Nat. Phys.* **13**, 369 (2017).
- [22] H. Yoo, R. Engelke, S. Carr, S. Fang, K. Zhang, P. Cazeaux, S. H. Sung, R. Hovden, A. W. Tsen, T. Taniguchi, K. Watanabe, G. Yi, M. Kim, M. Luskin, E. B. Tadmor, E. Kaxiras, and P. Kim, *Nat. Mater.* **18**, 448 (2019).
- [23] J. S. Aldena, A. W. Tsena, P. Y. Huanga, R. Hovdena, L. Brownb, J. Park, D. A. Muller, and P. L. McEuen, *Proc. Natl. Acad. Sci. USA* **110**, 11256 (2013).
- [24] P. Rickhaus, J. Wallbank, S. Slizovskiy, R. Pisoni, H. Overweg, Y. Lee, M. Eich, M. Liu, K. Watanabe, T. Taniguchi, V. Falko, T. Ihn, and K. Ensslin, *Nano Lett.* **18**, 6725 (2018).
- [25] S. G. Xu, A. I. Berdyugin, P. Kumaravadeivel, F. Guinea, R. Krishna Kumar, D. A. Bandurin, S. V. Morozov, W. Kuang, B. Tsim, S. Liu, J. H. Edgar, I. V. Grigorieva, V. I. Fal'ko, M. Kim, and A. K. Geim, *Nat. Commun.* **10**, 4008 (2019).
- [26] J. B. Qiao, L. J. Yin, and L. He, *Phys. Rev. B* **98**, 235402 (2018).
- [27] S. Huang, K. Kim, D. K. Efimkin, T. Lovorn, T. Taniguchi, K. Watanabe, A. H. MacDonald, E. Tutuc, and B. J. LeRoy, *Phys. Rev. Lett.* **121**, 037702 (2018).
- [28] T. Hou, Y. F. Ren, Y. J. Quan, J. Jung, W. Ren, and Z. H. Qiao, *Phys. Rev. B* **102**, 085433 (2020).
- [29] F. Zhang, A. H. MacDonald, and E. J. Mele, *Proc. Natl. Acad. Sci. USA* **110**, 10546 (2013).
- [30] W. Yao, S. A. Yang, and Q. Niu, *Phys. Rev. Lett.* **102**, 096801 (2009).
- [31] Y. T. Zhang, Z. H. Qiao, and Q. F. Sun, *Phys. Rev. B* **87**, 235405 (2013).
- [32] X. T. Bi, J. Jung, and Z. H. Qiao, *Phys. Rev. B* **92**, 235421 (2015).
- [33] M. Killi, S. Wu, and A. Paramekanti, *Phys. Rev. Lett.* **107**, 086801 (2011).
- [34] M. Zarenia, O. Leenaerts, B. Partoens, and F. M. Peeters, *Phys. Rev. B* **86**, 085451 (2012).
- [35] J. R. Anglin and A. Schulz, *Phys. Rev. B* **95**, 045430 (2017).
- [36] Z. H. Qiao, J. Jung, C. Lin, Y. F. Ren, A. H. MacDonald, and Q. Niu, *Phys. Rev. Lett.* **112**, 206601 (2014).
- [37] T. Hou, G. H. Cheng, W.-K. Tse, C. G. Zeng, and Z. H. Qiao, *Phys. Rev. B* **98**, 245417 (2018).
- [38] K. Wang, T. Hou, Y. F. Ren, and Z. H. Qiao, *Front. Phys.* **14**, 23501 (2019).
- [39] T. Hou, Y. Ren, Y. Quan, J. Jung, W. Ren, and Z. Qiao, *Phys. Rev. B* **101**, 201403(R) (2020).
- [40] J. Jung, F. Zhang, Z. H. Qiao, and A. H. MacDonald, *Phys. Rev. B* **84**, 075418 (2011).
- [41] C. Lee, G. Kim, J. Jung, and H. Min, *Phys. Rev. B* **94**, 125438 (2016).
- [42] M. Y. Wang, L. P. Liu, C.-C. Liu, and Y. G. Yao, *Phys. Rev. B* **93**, 155412 (2016).
- [43] S. G. Cheng, H. Liu, H. Jiang, Q. F. Sun, and X. C. Xie, *Phys. Rev. Lett.* **121**, 156801 (2018).
- [44] Y. F. Ren, J. J. Zeng, K. Wang, F. M. Xu, and Z. H. Qiao, *Phys. Rev. B* **96**, 155445 (2017).
- [45] M. Pelc, W. Jaskolski, A. Ayuela, and L. Chico, *Phys. Rev. B* **92**, 085433 (2015).
- [46] K. Wang, Y. F. Ren, X. Z. Deng, S. A. Yang, J. Jung, and Z. H. Qiao, *Phys. Rev. B* **95**, 245420 (2017).
- [47] W. Jaskolski, *Phys. Rev. B* **100**, 035436 (2019).
- [48] J. Klinovaja, G. J. Ferreira, and D. Loss, *Phys. Rev. B* **86**, 235416 (2012).
- [49] H. Pan, X. Li, F. Zhang, and S. A. Yang, *Phys. Rev. B* **92**, 041404(R) (2015).
- [50] J. Taylor, H. Guo, and J. Wang, *Phys. Rev. B* **63**, 245407 (2001).
- [51] D. Waldron, P. Haney, B. Larade, A. MacDonald, and H. Guo, *Phys. Rev. Lett.* **96**, 166804 (2006).
- [52] P. E. Blöchl, *Phys. Rev. B* **50**, 17953 (1994).
- [53] J. P. Perdew, J. A. Chevary, S. H. Vosko, K. A. Jackson, M. R. Pederson, D. J. Singh, and C. Fiolhais, *Phys. Rev. B* **46**, 6671 (1992).
- [54] G. Kresse and J. Furthmüller, *Comput. Mater. Sci.* **6**, 15 (1996).
- [55] G. Kresse and J. Furthmüller, *Phys. Rev. B* **54**, 11169 (1996).
- [56] G. Kresse and D. Joubert, *Phys. Rev. B* **59**, 1758 (1999).
- [57] M. U. Kahaly, S. P. Singh, and U. V. Waghmare, *Small* **4**, 2209 (2008).

- [58] J. Lahiri, Y. Lin, P. Bozkurt, I. I. Oleynik, and M. Batzill, *Nat. Nanotechnol.* **5**, 326 (2010).
- [59] Z. Y. Guan, Q. X. Li, and X. J. Wu, *Nano LIFE* **2**, 1240003 (2012).
- [60] J. F. Chen, Y. L. Han, X. H. Kong, X. Z. Deng, H. J. Park, Y. L. Guo, S. Jin, Z. K. Qi, Z. H. Lee, Z. H. Qiao, R. S. Ruoff, and H. X. Ji, *Angew. Chem., Int. Ed.* **55**, 13822 (2016).
- [61] S. Okada, T. Kawai, and K. Nakada, *J. Phys. Soc. Jpn.* **80**, 013709 (2011).
- [62] P. Y. Huang, C. S. Ruiz-Vargas, A. M. van der Zande, W. S. Whitney, S. Garg, J. S. Alden, C. J. Hustedt, Y. Zhu, J. Park, P. L. McEuen, and D. A. Muller, *Nature (London)* **469**, 389 (2011).
- [63] J. H. Warner, G.-D. Lee, K. He, A. W. Robertson, E. Yoon, and A. I. Kirkland, *ACS Nano* **7**, 9860 (2013).
- [64] M. Z. Liu, M. X. Liu, L. M. She, Z. Q. Zha, J. L. Pan, S. C. Li, T. Li, Y. Y. He, Z. Y. Cai, J. B. Wang, Y. Zheng, X. H. Qiu, and D. Y. Zhong, *Nat. Commun.* **8**, 14924 (2017).